One-dimensional acoustic models of horns and comparison with measurements

Thomas Hélie, Thomas Hézard, Rémi Mignot, Denis Matignon

ACTA ACUSTICA UNITED WITH ACUSTICA
Vol. 99 (2013) 960 – 974

DOI 10.3813/AAA.918675

One-Dimensional Acoustic Models of Horns and Comparison with Measurements

Thomas Hélie[1], Thomas Hézard[1], Rémi Mignot[2], Denis Matignon[3]
[1] IRCAM - CNRS UMR 9912, Sciences et Technologies de la Musique et du Son - UPMC, 1 place Igor Stravinsky, 75004 Paris, France. [thomas.helie, thomas.hezard]@ircam.fr
[2] Institut Langevin, ESPCI ParisTech, 10 rue Vauquelin, 75005 Paris, France. remi.mignot@espci.fr
[3] Université de Toulouse, ISAE 10, av. E. Belin. BP 54032, 31055 Toulouse Cedex 4, France. denis.matignon@isae.fr

Summary
Due to the simple properties of plane waves, non lossy straight pipes and their concatenation have been extensively used to derive digital waveguide synthesis and to compute acoustic immittances (input impedance, transmittance, etc) of wind instruments. This paper focuses on some possible refinements of such 1D wave propagation models, especially in the case of smooth horns. Four key points are examined: a refined curvilinear 1D horn equation, the smooth connection of constant-flared acoustic pipes, a radiation model consistent with spherical wavefronts, the effect of visco-thermal losses at the wall. They allow the definition of a complete model, from which a standard matrix formalism is recovered, as for plane or spherical waves. The comparison with measurements shows that each of these refinements is relevant, making one-dimensional models useful and efficient even for the quite sensitive case of brass instruments. Moreover, compared to the standard descriptions based on straight or conical pipes, the model proposed here gives accurate descriptions with only a few segments.

PACS no. 43.20.Mv,43.75.Ef,43.75.Fg

1. Introduction

For many wind instruments, one-dimensional (1D) models of acoustic bores are accurate enough for sound synthesis issues and for computing immittances (input impedance, transmittance, etc). Thus, descriptions based on planar or spherical waves propagating in piecewise straight or conical pipes have been extensively used [1, 2, 3, 4, 5, 6], including for the vocal tract [7, 8]. They allow the derivation of closed-form formulae from the bore profile, using a transfer matrix method and a radiation impedance load (see e.g. [9] for standard models and [10] for some comparison with measurements). However, discontinuous approximations of profiles involve impulse responses composed of pulse trains of Dirac measures, which are unrealistic for smooth bores. Similarly, continuous but non smooth approximations based on conical segments involve discontinuous pulse trains of damped exponentials. In the case of smooth flared horns, many segments are needed to weaken such artifacts.

This paper addresses the issue of improving accuracy, while preserving such 1D models and piecewise decompositions. For refinement, four points are examined:
(1) a horn equation based on an isobar map rectification;
(2) the smooth connection of constant-flared pipes;
(3) a radiation model which is consistent with (1);
(4) the effect of visco-thermal losses at the wall.
This allows the recovery of a transfer matrix method which is adapted to the computation of immittances of bores with a smooth profile. The complete model yields accurate results with only a few segments. Each of the four "ingredients" proves relevant. Moreover, as for plane waves in straight pipes, it still makes definitions of travelling waves and of digital waveguide-like structures possible.

The paper is organized as follows. Sections 2 to 5 are dedicated to the study of each ingredient, that is, the influence of: the choice of the wave-shape assumption in the horn equation (§ 2), the geometric regularity at junctions in piecewise segment modelling (§ 3), the radiation impedance (§ 4) and visco-thermal losses (§ 5). These studies are illustrated on the academic horn profile detailed in the Appendix. Section 6 presents results on a trombone bell, the profile and the input impedance of which have been measured.

Received 10 February 2012,
accepted 21 April 2013.

2. Ingredient 1: horn equation with curvilinear abscissa

2.1. Brief history summary and context

The first 1D model of the lossless acoustic propagation in axisymmetric pipes is due to [11, 12]. It is usually called

"horn equation" or *"Webster equation"* [13] and has been extensively investigated, witnessed in e.g. [14]. Its first version is based on planar waves but this assumption has been periodically revised. So, to preserve the orthogonality of the rigid motionless wall and wavefronts, Lambert [15] and Weibel [16] contest derivations based on planar waves and postulate spherical ones. The quasi-sphericity was experimentally confirmed for a horn profile in the low frequency range by Benade and Janson [17]. Later, Putland [18] pointed out that *every one-parameter acoustic field obeys a Webster equation* for particular coordinates. He also found that only planar, cylindrical and spherical waves could correspond to exact models. A similar result proved in [19, 20] states that the only static axisymmetric isobar maps on which waves can propagate correspond to these waves and to some modal maps. In spite of this limitation, some refined 1D models have still been looked for because of their simplicity (see e.g. [21, 22]): they make the computation of impedances easy and the frequency range that is not perturbed by transverse modes [23] is usually sufficiently large to study many wind musical instruments.

2.2. Remarks on the consistency between the geometry of isobars and the 1D horn equations

In this paper, we consider the model proposed in [19, 20]. This choice is motivated by its ability to regenerate several exact models and its consistency with the following statement. On the one hand, the geometric results and the observations compiled below are standard.

Property 1 (Isobars in axisymmetric waveguides)
For conservative propagation in axisymmetric pipes, some basic geometric properties of isobars are that:

(i) plane waves propagate in straight pipes (they are governed by $(\partial_z^2 - (1/c^2)\partial_t^2)p = 0$ where the space variable z denotes the axial abscissa);
(ii) spherical waves propagate in conical pipes (they are governed by $(\partial_r^2 + (2/r)\partial_r - (1/c^2)\partial_t^2)p = 0$ where r denotes the spherical abscissa);
(iii) isobars are orthogonal to the wall (except for null gradient of pressure, see [19, p.33] for a discussion);
(iv) according to [17], quasi-spherical isobars can be experimentally observed in the low frequency range;
(v) except for plane waves (i), spherical waves (ii) and a few other isolated cases, isobar profiles are generally time-varying (see [20, § II.C.]).

On the other hand, following [18], every 1D conservative propagation obeys a Webster horn equation, that is,

$$\left(\frac{1}{A(s)}\,\partial_s\big(A(s)\,\partial_s\big) - \frac{1}{c^2}\partial_t^2\right) p(s,t) = 0, \qquad (1)$$

where s and $s \mapsto A(s)$ denotes a space variable and a cross-section area, respectively.

However, the first models mentioned in § 2.1 are not consistent with all the properties 1 (i-v). More precisely, the original model [11, 12, 13] corresponds to $s = z$ and

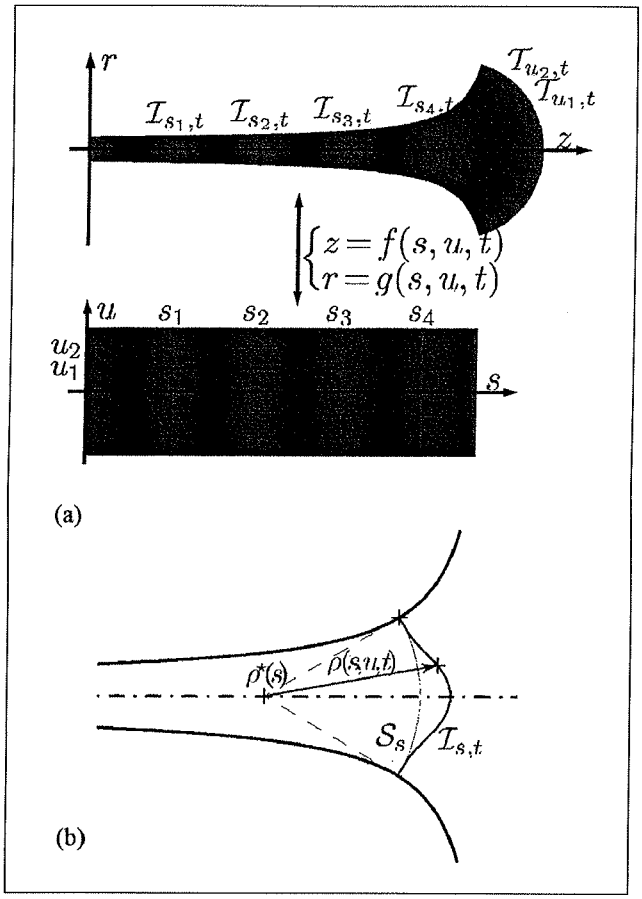

Figure 1. Isobar map rectification and local-in-space approximation near the wall. (a) isobar map rectification, (b) quasi-spherical approximation.

$A = \pi R^2$ where $z \mapsto R(z)$ denotes the local radius of the bore profile. The model is often written w.r.t. R as

$$\left(\partial_z^2 + \frac{2\,R'(z)}{R(z)}\partial_z - \frac{1}{c^2}\partial_t^2\right) p(z,t) = 0, \qquad (2)$$

or $$\left(\partial_z^2 - \frac{R''(z)}{R(z)} - \frac{1}{c^2}\partial_t^2\right) \big[R(z)\,p(z,t)\big] = 0. \qquad (3)$$

It corresponds to assuming plane waves and only restores property 1 (i). Models based on spherical wavefronts [15, 16] (s is a spherical abscissa and A describes the area of portions of spheres) or on ellipsoidal coordinates [21] restore properties 1 (i–iv) but are not consistent with (v).

2.3. Derivation of a 1D model consistent with properties 1(i-v)

2.3.1. Step 1: isobar wave equation

The first step consists in writing the wave equation for axisymmetric problems $\left[\partial_r^2 - \frac{1}{r}\partial_r + \partial_z^2 - \frac{1}{c^2}\partial_t^2\right] P(z,r,t) = 0$ in a rectified isobar map. Formally, this is achieved by using a coordinate transformation $z = f(s,u,t)$, $r = g(s,u,t)$ such that $P(f(s,u,t), g(s,u,t), t) = p(s,t)$ does not de-

pend on u: the space variable s is chosen such that it indexes isobars $\mathcal{I}_{s,t}$ (cf. Figure 1a). This leads to

$$\left[\alpha\,\partial_s^2 + \beta\,\partial_s + \gamma\,\partial_s\partial_t - \frac{1}{c^2}\partial_t^2\right]\widetilde{p}(s,t) = 0, \tag{4}$$

where α, β, γ are functions of (s,u,t).

Remark 1 (Isobar map parameterizations) Without loss of generality, the change of coordinates can be chosen such that: (i) (s,u) are orthogonal and directly oriented $(\arg[(\partial_u f + i\partial_u g)/(\partial_s f + i\partial_s g)] = \pi/2)$; (ii) $f(s,-u,t) = f(s,u,t)$, $g(s,-u,t) = -g(s,u,t)$ (symmetry w.r.t. the (Oz) axis, given by $u = 0$); (iii) $u = 1$ maps to the (motionless) bore profile described by some known (time-invariant) functions $f(s,u=1,t) = F(s)$, $g(s,u=1,t) = G(s)$.

According to the general formula given in [19, 20], for the choice of remark 1(i), coefficients are

$$\alpha = \frac{1-\xi_s^2}{\sigma_s^2}, \qquad \gamma = 2\frac{\xi_s}{c\,\sigma_s},$$
$$\beta = \frac{\sin\varphi}{g\,\sigma_s} + \frac{1-\xi_n^2}{\sigma_s^2}\left(\frac{\sigma_s\partial_u\varphi}{\sigma_u} - \partial_s\ln\sigma_s\right) - \frac{1}{2}\partial_s\frac{\xi_s^2-\xi_n^2}{\sigma_s^2} + \frac{1}{c}\partial_t\frac{\xi_s}{\sigma_s},$$

with $\sigma_s = \sqrt{(\partial_s f)^2 + (\partial_s g)^2}$, $\sigma_u = \sqrt{(\partial_u f)^2 + (\partial_u g)^2}$ (vector norms), $\varphi = \arg(\partial_s f + i\partial_s g)$ (angle) and $\xi_s = \frac{1}{c}[\partial_t f\cos\varphi + \partial_t g\sin\varphi]$, $\xi_n = \frac{1}{c}[-\partial_t f\sin\varphi + \partial_t g\cos\varphi]$ (Mach numbers).

2.3.2. Step 2: ideal motionless walls and quasi-spherical isobars

Exact derivations based on remark 1(i,iii) show that, on the wall $(u=1, z=F(s), r=G(s))$, coefficients in (4) are $\alpha(s,1,t) = 1/\left(F'(s)^2 + G'(s)^2\right)$, $\gamma(s,1,t) = 0$ and

$$\frac{\beta(s,1,t)}{\alpha(s,1,t)} = \partial_s\ln\left|\frac{G(s)}{F'(s)}\right| + \partial_s\ln\left|\partial_u g(s,u=1,t)\right|. \tag{5}$$

To obtain a 1D wave equation, an approximation is assumed in order to decouple the problems of the isobar *"shapes"* and *"values"*. The simplest one that is consistent with properties 1 (i-v) and that gives a closed formula for the coupling quantity $\partial_u g(s,u=1,t)$ is the following one.

Hypothesis 1 (Isobar quasi-sphericity at order 2) Denote $\rho^\star(s)$ the radius of the spherical isobar approximation (orthogonal to the wall) and $\rho(s,u,t)$ the length between the center of this sphere $\mathcal{S}_s$ and the isobar $\mathcal{I}_{s,t}$ at u (see Figure 1b). The relative deviation $\zeta = \rho/\rho^\star - 1$ satisfies $\partial_u^k\zeta(s,u=1,t) = 0$ for $k=0$ (contact) and $k=1$ (tangency of $\mathcal{S}_s$ and $\mathcal{I}_{s,t}$). This is still assumed at order $k=2$ (deviation slower than a parabola).

This hypothesis leads to the closed-form expression $\beta(s,1,t)/\alpha(s,1,t) = 2G'(s)/G(s)$. A closed formula is also obtained for the Euler equation [20, (53)], yielding a complete model.

Result 1 (Horn model with curvilinear abscissa ℓ) Hypothesis 1 provides a 1D acoustic model which is the same as for plane waves, except that the space variable $s = z$ is replaced by the *curvilinear abscissa* $s = \ell$ that measures the profile length (so that $\alpha(\ell,1,t) = 1$). The bore descriptions $z \mapsto R(z)$ and $\ell \mapsto \mathcal{R}(\ell)$ are linked by

$$\ell = L(z) = \int_0^z \sqrt{1 + \left[R'(z)\right]^2}\,\mathrm{d}z,$$
$$\mathcal{R}(\ell) = R\big(L^{-1}(\ell)\big). \tag{6}$$

The horn equation and the Euler equation are given by

$$\left(\partial_\ell^2 - \Upsilon(\ell) - \frac{1}{c^2}\partial_t^2\right)\left[\mathcal{R}(\ell)\,p(\ell,t)\right] = 0, \tag{7}$$

with $\Upsilon = \dfrac{\mathcal{R}''}{\mathcal{R}}$,

$$\rho\,\partial_t v(\ell,t) + \partial_\ell p(\ell,t) = 0. \tag{8}$$

2.4. Remarks, properties and validity

This model restores a Webster horn equation, in accordance with [18]. Its modification is concerned with the space variable (6) rather than replacing the cross-section area by e.g. that of $\mathcal{S}_s$ (Figure 1b). This is due to Hypothesis 1 which is local-in-space and does not require static spherical isobars, following property 1 (v). Moreover, (6)–(8) regenerate exact models for straight pipes ($\ell = z$, $R(z) = \mathcal{R}(\ell) = R_0$) and conical pipes ($\ell = z/\cos\theta$ ($\equiv r$ in property 1(ii)), $R(z) = z\tan\theta$, $\mathcal{R}(\ell) = \ell\sin\theta$). These cases correspond to $\Upsilon_\ell = 0$.

For non-straight pipes, the z-model is not exact: its validity is limited to the low frequency range $f \ll (c/\pi)\left(\int_0^Z \left[R'(z)\right]^2\mathrm{d}z\right)^{-1}$ (see [24, (7.159)]).

Property 2 (ℓ-model) Compared to the z-model, the ℓ-model modifies some practical features (see Figure 2):

(i) the equivalent pipe length is increased (as any local travel length: $L(z+\delta) - L(z) \geq \delta$ if $\delta \geq 0$),

(ii) the slopes are weakened as

$$\mathcal{R}'\big(L(z)\big) = R'(z)/\sqrt{1+R'(z)^2} \text{ so that } |\mathcal{R}'(\ell)| \leq 1$$

and that $\mathcal{R}'(\ell) = 1$ matches the vertical limit,

(iii) if a bore ends with a (possibly infinitesimal) cone ($\Upsilon_\ell = 0$ at $\ell = L$), the ℓ-model operates as a connection with ideal spherical waves for $\ell \geq L$,

(iv) the value and the shape of the flaring constant Υ are modified ($\Upsilon_z = R''/R$ in (3), $\Upsilon_\ell = \mathcal{R}''/\mathcal{R}$ in (7)),

(v) the locations of the peaks of immittances are modified in a non trivial way, as a consequence of (i-iv).

This is emphasized by the following acoustic feature.

Remark 2 (Local-in-space cutoff frequency $f^\star$) When the flaring parameter Υ is positive, it can be mapped to a local-in-space cutoff frequency $f^\star = \frac{c}{2\pi}\sqrt{\Upsilon}$ below which travelling waves are evanescent [17].

The differences between z- and ℓ-models increase with the deviation $L(z) - z$. According to (6), this occurs when the profile slope R' moves away from 0 (see Figure 2).

The validity of a 1D horn equation is limited in practice to frequencies for which no transverse modes can be excited. An order of magnitude is given for the case of a straight pipe with radius $R_{max} = \max_{\ell\in[0,L]} \mathcal{R}(\ell)$

$$f < f^+ \text{ with } f^+ = \frac{K^+}{R_{max}}, \quad K^+ = \frac{1.84\,c}{2\pi} \approx 100\,\text{m/s}. \quad (9)$$

Another validity condition is that $|\Upsilon|$ be small enough to be close to exact models ($\Upsilon = 0$).

Hypothesis 1 does not provide quantitative validity criteria but section 6 gives a comparison between models and measurements.

In the following, s denotes the complex Laplace variable.

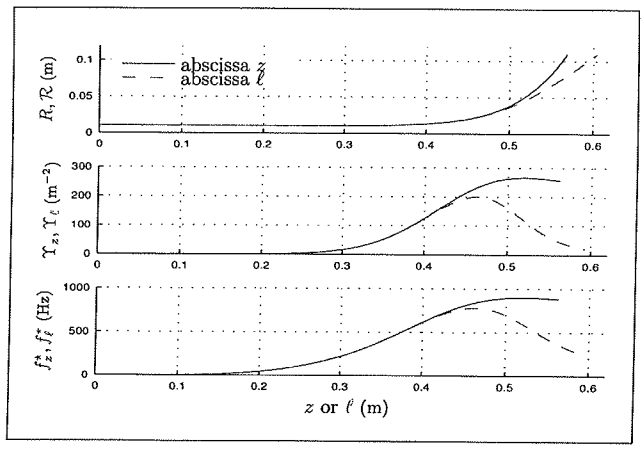

Figure 2. Comparison of the z-models R, $\Upsilon_z = R''/R$, $f_z^\star = c\sqrt{\Upsilon_z}/(2\pi)$, (–) to the ℓ-models $\mathcal{R}$, $\Upsilon_\ell = \mathcal{R}''/\mathcal{R}$, $f_\ell^\star = c\sqrt{\Upsilon_\ell}/(2\pi)$, - -) for the toy-profile (A1) in appendix A1.

3. Ingredient 2: smooth connection of Υ-constant segments

3.1. History summary and problem statement

Piecewise approximations have been first based on straight pipe segments (Figure 3a). This yields simple transfer matrices from which a *Kelly-Lochbaum structure* is obtained, that is, a digital waveguide structure involving *propagators* (delays) and a single *reflection* function at each junction [1, 25]. The deduced *auto-regressive* filters have been extensively used for real-time sound synthesis, especially for the vocal tract [7, 8]. But, this first model introduces several approximations: (1) profile discontinuities, (2) frequency-independent radiation, (3) no viscothermal losses. The first one involves instantaneous reflections. It makes the impulse response (IR) of *immittances* composed of Dirac pulses rather than the expected smooth ones. This artifact is concealed (regularized IRs) if approximations (2) or (3) are dropped. It is also why the space discretization is usually chosen such that the pulses are synchronized with the sampling period. As an alternative, conical segments have been used to increase the regularity (Figure 3b). These segments significantly improve the acoustic results, if the radius deviation and their slope variation are small enough [26, 4, 6, 10]. It yields a Kelly-Lochbaum structure for C^0-junctions [3]. Some smooth profiles have also been studied (e.g. Bessel horns [17], exponential horns [27], see also [28]).

Here, the C^1-regular junction of Υ-constant segments is proposed (same regularity as cubic splines, but segments are not polynomial because of the acoustic model). One issue addressed here is: which degree of regularity can be reached on the acoustic impulse responses?

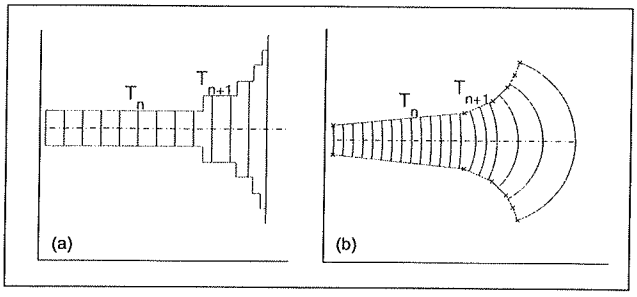

Figure 3. Standard piecewise approximations.

3.2. Transfer matrix method for piecewise Υ-constant profiles

Consider a segment on $\ell \in (a, b)$ governed by (7-8) with constant parameter $\Upsilon < 0$ (convex bore), $\Upsilon = 0$ (straight, conical) or $\Upsilon > 0$ (flared).

This causal problem is solved in the Laplace domain $\mathbb{C}_0^+ = \{s \in \mathbb{C} \,|\, \Re e(s) > 0\}$ (see [19, p.63] and [29]).

Result 2 (Transfer matrix $\mathbf{T}_{b,a}$ of one segment) Denote $X_\ell(s) = \left[P(\ell, s)\,,\, U(\ell, s)\right]^T$ the acoustic state inside the Υ-constant segment, where P and U are the Laplace transforms of $t \mapsto p(\ell, t)$ and $t \mapsto \pi\mathcal{R}(\ell)^2 v(\ell, t)$ (assumed to be zero for $t < 0$), respectively. Then,

$$X_b(s) = \mathbf{T}_{b,a}(s)\, X_a(s), \quad (10)$$

where

$$\mathbf{T}_{b,a}(s) = \Lambda_{b^-}(s)\mathbf{M}_{b,a}(s)\Lambda_{a^+}(s)^{-1}$$

has determinant one, $\Lambda_\ell(s) = \text{diag}\left(\frac{1}{\mathcal{R}(\ell)}, \frac{\pi\mathcal{R}(\ell)}{\rho s}\right)$ and $\left[\mathbf{M}_{b,a}(s)\right]_{i,j} = \left(V_{i,j}(s)\right)^T \Phi\big((b-a)\Gamma(s)\big)$ with

$$V_{11} = [1\,,\, \sigma(a^+)]^T, \qquad V_{12} = [0\,,\, -(b-a)]^T,$$
$$V_{21} = [\frac{\sigma(b^-) - \sigma(a^+)}{b-a}\,,\, \frac{\sigma(a^+)\sigma(b^-) - (b-a)^2\Gamma^2}{b-a}]^T,$$
$$V_{22} = [1\,,\, -\sigma(b^-)]^T,$$

$\Phi(z) = [\cosh z\,,\, \sinh z/z]^T$ and $\sigma = \mathcal{R}'/(\mathcal{R}/(b-a))$ (dimensionless ratio of slopes). Function Γ is the principal value of the square-root of

$$\Gamma(s)^2 = \left(\frac{s}{c}\right)^2 + \Upsilon. \quad (11)$$

Matrix $T_{b,a}$ defines a stable causal operator for positive profiles, that is, if $\mathcal{R}(a) > 0$, $\mathcal{R}(b) > 0$ and $(b-a)^2\mathrm{Y} > -\pi^2$.

Remark 3 (Wavenumber) The wavenumber k is such that $\mathrm{i}k = \Gamma(\mathrm{i}\omega)$ where ω is the angular frequency. For straight and conical pipes ($\mathrm{Y} = 0$), it becomes $k = \omega/c$.

The acoustic connection of N segments (located by $\ell_0 < \ell_1 < \cdots < \ell_N$) is achieved by imposing the continuity of X_ℓ at junctions. This yields the transfer matrix method

$$X_{\ell_N}(s) = \mathbf{T}_{\ell_N,\ell_0}(s)\, X_{\ell_0}(s), \tag{12}$$

$$\mathbf{T}_{\ell_N,\ell_0} = \mathbf{T}_{\ell_N,\ell_{N-1}}\, \mathbf{T}_{\ell_{N-1},\ell_{N-2}} \cdots \mathbf{T}_{\ell_1,\ell_0}, \tag{13}$$

which exactly restores the standard results for straight and conical pipes (see Figure 3 and e.g. [8], [24, p.293]).

Remark 4 (Continuous profiles)
For C^0-junctions, (12) takes the simpler form

$$\mathbf{T}_{\ell_N,\ell_0} = \Lambda_{\ell_N}\mathbf{M}_{\ell_N,\ell_0}\Lambda_{\ell_0}^{-1}$$
$$\text{with}\quad \mathbf{M}_{\ell_N,\ell_0} = \mathbf{M}_{\ell_N,\ell_{N-1}}\, \mathbf{M}_{\ell_{N-1},\ell_{N-2}} \cdots \mathbf{M}_{\ell_1,\ell_0}.$$

3.3. Kelly-Lochbaum structure for flared horns

Piecewise cylindrical ⓐ, conical ⓑ and Y-constant ⓒ segments can be described by digital waveguides (Figure 4): they are composed of pairs of *travelling operators* (called *propagators*) with transfer function $W_n(s) = \exp\left[-(\ell_n - \ell_{n-1})\Gamma_n(s)\right]$ which are interconnected through two-port operators C_n at junctions, and connected to load transfer functions at boundaries [1, 2, 3, 5, 30, 31, 32, 33].

In cases ⓐ–ⓑ ($\mathrm{Y}_n = 0$), propagators are simple delays $D_n(s) = \exp(-\tau_n s)$ with $\tau_n = (\ell_n - \ell_{n-1})/c$. In case ⓒ, the dispersion function $G_n(s) = W_n(s)/D_n(s) = \exp(\tau_n(s - c\Gamma_n(s)))$ corresponds to a (non-delayed) causal stable operator, only if $\mathrm{Y} \geq 0$ [30].

Computing its IR yields [34, p.498], for all $\mathrm{Y} \geq 0$,

$$g_n(t) = \delta(t) - 1_{t>0}(t)\, c\tau_n\sqrt{\mathrm{Y}_n}\frac{J_1\left(c\sqrt{\mathrm{Y}_n}\sqrt{t(t+2\tau_n)}\right)}{\sqrt{t(t+2\tau_n)}}, \tag{14}$$

where J_1 is the Bessel function of the first kind of order 1.

Moreover, for sufficiently regular profiles, the following property of C_n comes out (see [2, 3, 31] and [33, § 4]).

Property 3 (Kelly-Lochbaum factorization)
When the geometric regularity allowed by piecewise descriptions ⓐ–ⓒ is maximal (discontinuous for ⓐ, continuous for ⓑ, C^1-regular for ⓒ), each two-port function $C_n(s)$ can be realized with only one reflection transfer function $K_n(s)$ and three sums (Figure 5).

This factorization significantly reduces the computation load of simulations for sound synthesis purposes.

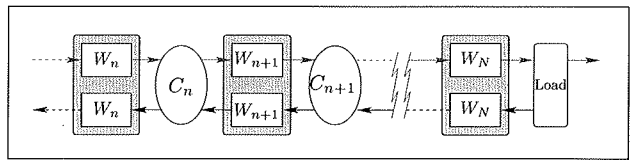

Figure 4. Waveguide decomposition: propagators W_n control "decoupled waves" $w^{\pm}(\ell, t)$ inside the n-th segment; operators C_n process the reflected and transmitted parts at junctions.

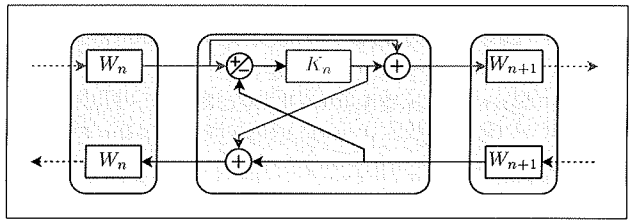

Figure 5. Kelly-Lochbaum structure: junction C_n.

3.4. Considerations on pulse trains and regularity

Consider a smooth bore with $\mathrm{Y} \geq 0$ loaded by a frequency-independent radiation or an infinitely-long last segment. Then, the following property is satisfied.

Property 4 The impulse response regularity of immittances of ⓐ–ⓒ is fixed by that of reflection functions K_n.

Proof: For cases ⓐ–ⓑ, propagators reduce to delays D_n and the result is straightforward. For case ⓒ, $G_n = W_n/D_n$ contains a direct gain 1 (δ in equation 14), yielding the result.

Table I recalls reflection function formulae and illustrates a caricature approximation of a flared profile with two segments. The analysis of these reflection functions yields the following result.

Result 3 (Impulse response regularity) For a smooth flared profile, C^1-regular junctions of Y-constant segments define the simplest piecewise-approximation that preserves the IR continuity, independently of the number of segments and the load impedance.

Proof: The IR discontinuity of cases ⓐ–ⓑ is straightforward: for ⓐ, the impulse response of the reflection corresponds to a Dirac pulse; for ⓑ, it corresponds to a causal damped exponential (one-pole filter in the Laplace domain) which is discontinuous at $t = 0$. Now, for ⓒ,

$$K_1^{ⓒ}(s) = \frac{\Gamma_1(s) - \Gamma_2(s)}{\Gamma_1(s) + \Gamma_2(s)} = \frac{\mathrm{Y}_1 - \mathrm{Y}_2}{(\Gamma_1(s) + \Gamma_2(s))^2}$$
$$= \frac{\mathrm{Y}_1 - \mathrm{Y}_2}{4(s/c)^2} + \mathcal{O}(\frac{1}{s^4})$$

as $s \to +\infty$. Hence, from the initial value theorem, $k_1(0^+) = \lim_{x\to+\infty} xK_1(x) = 0$ and $k_1'(0^+) = \lim_{x\to+\infty} x^2K_1(x) = (\mathrm{Y}_1 - \mathrm{Y}_2)/2$. Since $k_1(t)$ has no jump at $t = 0$ and k_1' has one, the IR regularity is C^0 but not C^1, which concludes the proof.

Table I. Regularity of the reflection functions involved in Kelly-Lochbaum structures w.r.t. the regularity of geometry. First line: Approximation of $\mathcal{R}^\dagger$ with two segments ($\ell_0 = 0.3$, $\ell_1 = 0.4$, $\ell_2 = 0.5$).

	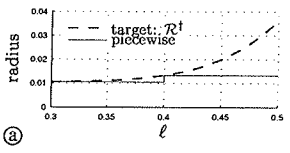	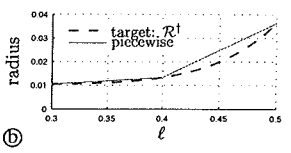	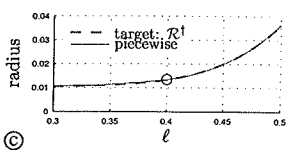
Profile regularity	discontinuous (straight pipes)	continuous (C^0) (conical pipes)	Smooth (C^1) (Y-constant)
$K_1(s)$	$(A_1 - A_2)/(A_1 + A_2)$	$\alpha_1/(s - \alpha_1)$	$(\Gamma_1(s) - \Gamma_2(s))/(\Gamma_1(s) + \Gamma_2(s))$
$k_1(t)$	$\big((A_1 - A_2)/(A_1 + A_2)\big)\delta(t)$	$\alpha_1 \exp(\alpha_1 t)\, 1_{t\geq 0}$	no closed-form solution
Jump at $t = 0$	infinite	$\alpha_1 = (c/2)\big(\mathcal{R}'(\ell_1^-) - \mathcal{R}'(\ell_1^+)\big)/\mathcal{R}(\ell_1)$	0
IR regularity	Dirac type	discontinuous	continuous (C^0)

Remark 5 (Piecewise conical approximation)
Nearly-continuous IR can be obtained by using C^0-regular junctions of cones and increasing the number of segments so that the mesh is refined and that coefficients $\alpha_n = c(\mathcal{R}'(\ell_n^-) - \mathcal{R}'(\ell_n^+))/(2\mathcal{R}(\ell_n))$ become small enough.

A conjecture for higher degrees of regularity is that a C^k-regular profile corresponds to a C^{k-1}-regular impulse response.

Note that, in the cases ⓐ–ⓑ, defining N segments from a target profile $\mathcal{R}$ is obtained by evaluating $\mathcal{R}$ at chosen abscissa $\ell_{n=0,\ldots,N}$. On the contrary, deriving a C^1-regular piecewise Y-constant decomposition is not easy. A tool which is specifically dedicated to optimize case ⓒ is used in this paper: it is detailed in [35].

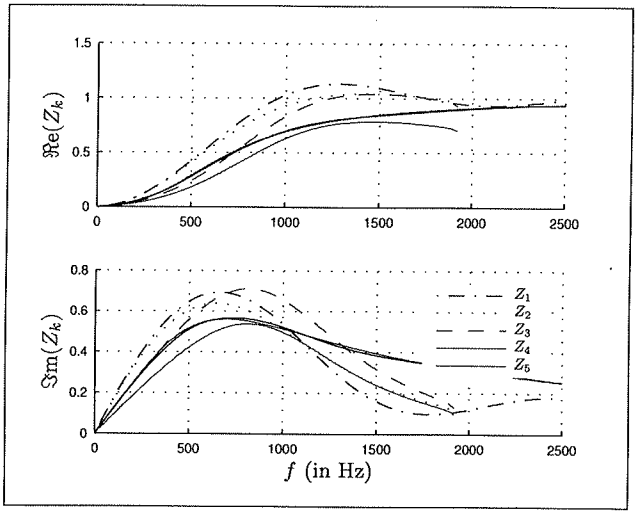

Figure 6. Comparison of radiation impedances for $R^\dagger$ at $z^\star$.

4. Ingredient 3: radiation impedance

4.1. History summary and context

The radiation impedance balances the energy which is confined in the pipe (a) and the radiated part (b). In the frequency range where phenomenon (a) dominates, the quality of resonances is high (making self-sustained oscillations and note emissions easier). Tuning the trade-off between these quality factors and the radiated sound power (especially for modern instruments) makes the study of impedances and their cutoff frequency crucial.

The first models used for wind instruments were based on planar pistons or straight pipes with various flange configurations. They can be described by

$$\frac{P_L}{V_L} = Z_{\text{rad}} = \rho c\, Z,$$

where the transfer function Z is dimensionless and is usually given w.r.t $ka = (2\pi f/c)a$ (a is the radius of the pipe and k is the wavenumber).

The difference between piston and pipe models is whether or not evanescent modes are taken into account. The most used models are (see Figure 6):

(Z_1) a flanged circular piston

$$Z_1 = 1 - \frac{2J_1(2ka)}{2ka} + \mathrm{i}\frac{2H_1(2ka)}{2ka},$$

where J_1 and H_1 are the first kind Bessel function and the Struve function of order 1, respectively [34]. The sign of the imaginary part is obtained by choosing a decomposition into mono-chromatic signals with the convention $\exp(2\mathrm{i}\pi ft)$ which is consistent with the Fourier and Laplace transforms with $s = 2\mathrm{i}\pi f$.

(Z_2) a flanged circular pipe [9, (9)], [36],

(Z_3) an unflanged pipe [37, (V.16)],

(see [9] for a comparison with their computations, [38] for an unflanged planar piston, [39] for the influence of the wall thickness and [40, 41] for other generalizations).

However, these models are not well-suited to flared horns, especially when the angle θ_0 of the tangent cone at the horn output is obtuse (see Figure 7). To account for spherical wavefronts, a corrected version of Z_3 with factor A_p/A_s has been proposed in [26] ($A_p = \pi\mathcal{R}^2 = \pi(r_0 \sin\theta_0)^2$ and $A_s = 2\pi r_0^2(1 - \cos\theta_0) = 2\pi\mathcal{R}^2/(1 + \cos\theta_0)$ are respectively the planar and spheri-

cal radiating areas). It yields

$$Z_4 = \frac{A_p}{A_s} Z_3 = \frac{1+\cos\theta_0}{2} Z_3,$$

with $\theta_0 \approx 59.2°$ for the profile $R^\dagger$ at $z = z^\star$ (defined in the Appendix). This model is consistent with energy conservation and mass conservation. It gives an exact result on $\Re\mathrm{e}(Z_4)$ in the low frequency limit. This impedance (see Figure 6) has been quite often used for bell modelling (see e.g. [4]).

To refine the effect of spherical wavefronts, the model Z_5 restated and analyzed here is one of [42]. It is based on a pulsating portion of a sphere. Following some comparison with measurements in [10], these refinements are significant in the case of a bell, especially beyond the cut-off frequency.

4.2. Model Z_5 and properties

Consider a sphere with radius r_0, whose part S_0 ($\theta \le \theta_0$, see Figure 7) is animated with velocity V_0 and the other one is motionless.

Under lossless linear acoustic assumptions and using spherical harmonic decompositions, the transfer function in the Fourier domain between $V_0(f)$ (f denotes the frequency) and the pressure field $P_{r_0,\theta_0}(f, r, \theta)$ in the external space ($r \ge r_0$) is found to be

$$\frac{P_{r_0,\theta_0}(r_0,\theta,f)}{V_{\theta_0}(\theta,f)} = \rho c\, H_{\theta_0}\Big(\frac{r}{r_0}, \theta, \frac{r_0 f}{c}\Big),$$

where $$H_{\theta_0}(\xi,\theta,\nu) = -\mathrm{i}\sum_{n=0}^{+\infty} \mu_n(\theta_0)\mathbb{P}_n(\cos\theta)\frac{h_n(2\pi\xi\nu)}{h_n'(2\pi\nu)},$$

$$\mu_n(\theta_0) = \frac{\mathbb{P}_{n-1}(\cos\theta_0) - \mathbb{P}_{n-1}(\cos\theta_0)}{2}, \quad \mathbb{P}_{-1}(X) = 1,$$

and, for $n \ge 0$, $\mathbb{P}_n$ and h_n denote the Legendre polynomials and the outgoing spherical Hankel functions, respectively.

The dimensionless impedance on S_0 is then characterized by $H_{\theta_0}(\xi,\theta,\nu)$ with $\xi = 1$.

Remark 6 (Reduced frequency ν)
In H_{θ_0}, the reduced frequency $\nu = f r_0/c = k r_0/(2\pi)$ is proportional to the sphere radius r_0 (in place of the pipe radius a in $Z_{1,2,3,4}$).

To make this impedance consistent with the 1D quasi-spherical model, its dependency w.r.t. θ must be removed. The approximation which minimizes the mean-square error over S_0 is the average on S_0. Its computation yields

$$Z_{\theta_0}(\nu) = -\frac{2\mathrm{i}}{1-\cos\theta_0}\sum_{n=0}^{+\infty}\frac{\big(\mu_n(\theta_0)\big)^2}{2n+1}\frac{h_n(2\pi\nu)}{h_n'(2\pi\nu)}.$$

As a result [42, see (24) and Figure 3c], the error is negligible in the very low frequency range ($\nu \ll 1$). The maximal error w.r.t. ν is a decreasing function of θ_0, so that Z_{θ_0} is a better approximation for large angles than for small ones.

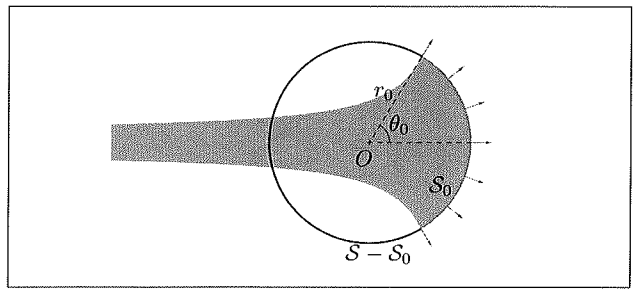

Figure 7. Flared horn radiation approximation.

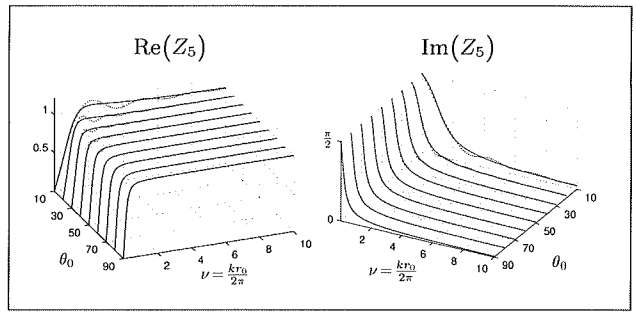

Figure 8. Impedance averaged on S_0 (...) and second order model Z_5 (-).

Moreover, Z_{θ_0} can be approximated by simpler models (denoted (M1,2,3) in [42, § 4]), the parameters of which have also been optimized for the mean-square error over S_0. Model (M2) is detailed below and displayed in Figure 8: it furnishes a good trade-off between the complexity and the accuracy for most of brass instruments.

Result 5 (Radiation impedance Z_5) For small angles θ_0, Z_{θ_0} is close to model Z_1 (flanged piston) which includes characteristic ripples. For angles θ_0 larger than about 55° (most of brass instruments), these ripples disappear and Z_{θ_0} is accurately approximated by the following second order model where the introduced error is negligible w.r.t. to that due to the average on S_0:

$$Z_5 : \nu = \frac{kr_0}{2\pi} \longmapsto \frac{\mathrm{i}\alpha\frac{\nu}{\nu_c} - \big(\frac{\nu}{\nu_c}\big)^2}{1 + 2\mathrm{i}\xi\frac{\nu}{\nu_c} - \big(\frac{\nu}{\nu_c}\big)^2}, \tag{15}$$

with the positive parameters, for $0 \le \theta_0 \le \frac{\pi}{2}$ (in radians),

$$\begin{aligned}
\xi(\theta_0) &= 0.0207\theta_0^4 - 0.144\theta_0^3 + 0.221\theta_0^2 \\
&\quad + 0.0799\theta_0 + 0.72, \\
\alpha(\theta_0) &= \big[0.1113\theta_0^5 - 0.6360\theta_0^4 + 1.162\theta_0^3 \\
&\quad - 1.242\theta_0^2 + 1.083\theta_0 + 0.8788\big]^{-1}, \\
\nu_c(\theta_0) &= \big[-0.198\theta_0^5 + 0.2607\theta_0^4 - 0.424\theta_0^3 \\
&\quad - 0.07946\theta_0^2 + 4.704\theta_0 + 0.022\big]^{-1}.
\end{aligned}$$

This impedance has the following properties.

Table II. Physical constants in the air and characteristic constants (extracted from [24, p.212], $T_0 = 273.16$ K is the absolute temperature at 0 Celsius degree, $T = 298.66$ K). Sound speed c, air density ρ, viscosity μ, thermal conductivity[2] κ, specific heat capacity at constant pressure C_P, heat capacity ratio γ, specific heat capacity at constant volume C_V, Viscous characteristic length (5.133) p.210 ℓ_v, Prandtl number P_r, Thermal characteristic length ℓ_t.

Formula	Accuracy	Value
$c = 331.5\sqrt{T/T_0}$	±0.015%	346.63 m/s
$\rho = 1.2929\,T_0/T$	±0.01%	1.18 Kg/m^3
$\mu = 1.708\cdot 10^{-5}$ $(1+0.0029(T-T_0))$	±2%	$1.834\cdot 10^{-5}$ kg/m/s
$\kappa = 0.0241$ $(1+0.0033(T-T_0))$	±9%	0.0261 J/m/s/K
$C_P = 0.24$	±0.1%	0.24 Cal/g/°C
$\gamma = 1.402$	±0.1%	1.402
$C_V = C_P/\gamma$	±0.1%	0.1712 Cal/g/°C
$\ell_v = \mu/(\rho c)$	±2%	$4.4751\cdot 10^{-8}$ m
$P_r = 0.71$	×	0.71
$\ell_t = \ell_v/P_r$	×	$6.303\cdot 10^{-8}$ m

Property 5 Model Z_5 is physically relevant:

(i) it defines a causal stable passive impedance,

(ii) it has the right asymptotic acoustic behaviours, $\lim_{\nu\to 0^+} Z_5(i\nu) = 0$ and $\lim_{\nu\to+\infty} Z_5(i\nu) = 1$.

Moreover, its cutoff frequency (such that $|Z_5|^2 = 1/2$) is

(iii) $f_c^{rad} = (c/r_0)\nu_c\sqrt{\sqrt{1+\beta^2}-\beta}$ where $\beta = 1+\alpha^2-2\xi^2$.

Proof: Equation (15) is also available in the complex Laplace domain $\Re e(s) > 0$ *with* $s = 2i\pi\nu$.
For all angles $\theta_0 \in [0, \pi/2]$, *its poles* $s = 2\pi\nu_c(-\xi \pm i\sqrt{1-\xi^2})$ *have a negative real part, from which the stability is deduced. Computing* $\Re e(Z_5)$ *yields* $X^2(2\alpha\xi - 1 + X^2)/[(1-X^2)^2 + (2\xi X)^2]$ *with* $X = \nu/\nu_c$. *It is negative for all* X, *if* $2\alpha\xi - 1 \geq 0$.
Now, $\min_{\theta_0}\big(2\alpha(\theta_0)\xi(\theta_0)\big) \geq 1.2$, *proving the passivity. (ii) is straightforward. Finally, straightforward derivations show that* $|Z_5|^2 - 1/2$ *is zero if* $X^4 + 2\beta X^2 - 1$. *The only positive root is* $X = \sqrt{-\beta + \sqrt{1+\beta^2}}$ *from which (iii) is deduced.*

For the physical constants and the (trombone) parameters given in Tables II and III, (iii) yields $f_c^{rad} \approx 848$ Hz. Moreover, Z_5 is consistent with the mass and the energy conservation principles (as Z_4) since, numerically and according to [42, § 4.4], $\lim_{\nu\to 0} \Re e\big(Z_5(i\nu)\big)/(2\pi\nu)^2 \approx (1-\cos\theta_0)/2$.

[2] Note that the thermal conductivity $\kappa = 5.77\cdot 10^{-5}\big(1+0.0033(T-T_0)\big)$ Cal/cm/s/°C given in [24] has been converted into J/m/s/K using the thermochemical calorie 1 Cal$_{th}$ ≈ 4.184 J.

Table III. Mesh description of the horn of a trombone Courtois 155R: z_m is the axial position, ℓ_m is the corresponding length of the profile from z_0 to z_m, R_m is the radius of the profile.

index m	z_m (mm)	ℓ_m (mm)	R_m (mm)
0	0.0	0.0000	10.4
1	66.5	66.5000	10.4
2	153.0	153.0113	11.8
3	198.4	198.4247	12.9
4	266.5	266.5570	15.0
5	315.0	315.0868	16.7
6	364.3	364.4315	18.8
7	400.0	400.1875	20.8
8	418.4	418.6266	22.0
9	431.8	432.0717	23.1
10	442.5	442.8387	24.3
11	454.6	455.0441	25.9
12	463.7	464.2511	27.3
13	472.9	473.5892	28.9
14	480.5	481.3558	30.5
15	488.0	489.0461	32.2
16	492.4	493.5815	33.3
17	496.7	498.1356	34.8
18	501.3	502.9439	36.2
19	505.4	507.2451	37.5
20	508.4	510.4762	38.7
21	510.8	513.1163	39.8
22	514.2	516.9176	41.5
23	518.3	521.5705	43.7
24	521.4	525.1552	45.5
25	524.0	528.3755	47.4
26	526.7	531.7355	49.4
27	530.8	536.9365	52.6
28	534.4	541.5593	55.5
29	537.8	546.3676	58.9
30	541.2	551.1759	62.3
31	543.9	555.2120	65.3
32	546.8	559.6808	68.7
33	550.4	565.6808	73.5
34	553.0	570.2851	77.3
35	555.8	575.2500	81.4
36	558.0	580.1694	85.8
37	560.8	585.3847	90.2
38	563.3	591.2448	95.5
39	565.4	597.8855	101.8
40	568.0	606.4879	110.0

5. Ingredient 4: visco-thermal losses

5.1. History summary and context

Kirchhoff, first, has introduced thermal conduction effects, extended the Stoke's theory and derived some basic solutions in free space and in a pipe. He gave the exact general dispersion relation for a cylinder for axisymmetric problems [43] (see [44, eq. (56)]) for non symmetric versions). Simplified models have also been proposed: separated viscous and thermal boundary layers (by Zwikker and Kosten [24, p.210], see [45, 46] for validity conditions), and the Cremer equivalent wall admittance for plane waves, which depends on the incidence angle on the wall and coincides

with the Kirchhoff result for rectangular waveguides if the boundary layer thickness is much smaller than the rectangle lengths. Propagation models based on this admittance and plane wave approximations have been derived. They include a damping term involving a fractional time derivative (see the Lokshin equation [47, 48] and [49]). Closed-form solutions of the Lokshin equation have been derived in [50, 51]. The model considered here is an extension of result 1.

5.2. Introducing visco-thermal losses in the curvilinear horn model and Y-constant segments

Adapting hypothesis (H1) in § 2 to the case of walls with a Cremer wall admittance, a perturbed curvilinear version of (7) is obtained (see [20]). It is given by

$$\left(\partial_\varrho^2 + 2\frac{\mathcal{R}'(\varrho)}{\mathcal{R}(\varrho)}\partial_\varrho - \frac{1}{c^2}\partial_t^2 - \frac{2\varepsilon(\varrho)}{c^{\frac{3}{2}}}\partial_t^{\frac{3}{2}}\right)p(\varrho,t) = 0. \quad (16)$$

In the last term, $\partial_t^{3/2}$ denotes a fractional time derivative (see e.g. [50] and references therein) and coefficient ε is given by $\varepsilon(\varrho) = \varepsilon^\star\sqrt{1-\mathcal{R}'(\varrho)^2}/\mathcal{R}(\varrho)$ where $\varepsilon^\star = \sqrt{l_v}+(\gamma-1)\sqrt{l_t} \approx 3.125\cdot10^{-4}\ \mathrm{m}^{1/2}$ according to the physical constants given in Table II (Kirchhoff's formula).This equation is sometimes called the "Webster-Lokshin" equation, because the "Webster equation" is recovered for $\varepsilon = 0$ and the "Lokshin equation" is recovered for $R' = 0$.

The complete model is (8), (16). It governs the propagation of the acoustic state out of the visco-thermal boundary layers.

Remark 6 (planar wave approximation)
A similar model has been derived in [49], assuming plane waves. It leads to (16), in which ϱ, $\mathcal{R}(\varrho)$ and $\varepsilon(\varrho)$ are replaced by z, $R(z)$ and the loss coefficient $\varepsilon(z) = \varepsilon^\star/R(z)$ which only depends on the profile radius (but not on its slope).

Consider Y-constant segments (indexed by $n = 1,\dots N$) on which $\varrho \mapsto \varepsilon(\varrho)$ is approximated by its mean value, namely,

$$\frac{\varepsilon_n}{\varepsilon^\star} = \frac{1}{\varrho_n - \varrho_{n-1}}\int_{\varrho_{n-1}}^{\varrho_n}\frac{\sqrt{1-\mathcal{R}'(\varrho)^2}}{\mathcal{R}(\varrho)}\,\mathrm{d}\varrho$$

(or, according to remark 3, $\varepsilon_n/\varepsilon^\star = [1/(z_n - z_{n-1})]\cdot\int_{z_{n-1}}^{z_n}(1/R(z))\,\mathrm{d}z$ for the planar wave approximation). This yields the same transfer matrix as in result 2 where (11) is replaced by

$$\Gamma_n(s)^2 = \left(\frac{s}{c}\right)^2 + 2\varepsilon_n\left(\frac{s}{c}\right)^{\frac{3}{2}} + \mathrm{Y}_n. \quad (17)$$

Moreover, the following result has been proved, even for constant piecewise profiles [50, 51] (Table Ia, Figure 9a).

Result 5 (Regularization and long-memory)
The fractional derivative in (16) regularizes the IR of immittances and introduces some "long-memory effects":

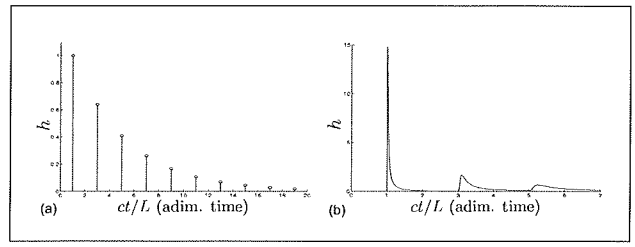

Figure 9. Pressure transmission IR h ($p(L,\cdot) = h * p(0,\cdot)$) for a straight pipe loaded with a constant positive impedance. (a): no losses; $\varepsilon = 0$ [50, figure 5.5], (b) losses; $\varepsilon = 0.25$ [50, figure 6.7b]

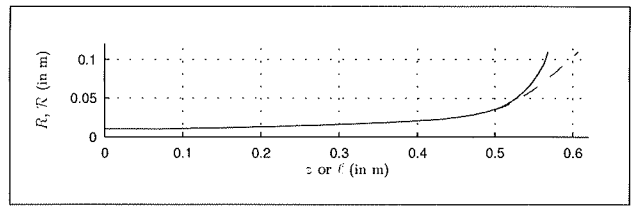

Figure 10. Measured profile (-) and corresponding ϱ-profile (- -). *See also Table III.*

(i) Dirac pulses are transformed into C^∞-pulses,
(ii) these pulses decay more slowly than any decreasing exponential (long-memory),
(iii) the modes of such fractionally-damped systems are not reduced to standard Q-resonances.

Remark 7 (Modes in fractional systems)
In (iii), the modal dynamics is not of exponential-type but of Mittag-Leffler type [52], with long-memory decays. Their IR functions can be decomposed into a finite sum (poles) and an infinite-continuous sum (integrals on cuts) of first order models [30, 51, 53, 54].

The regularization and the long-memory effects also appear in cases ⓑ–ⓒ (see [30, Figure 10] and [33, Figure 17]).

6. Application and results

In this section, results based on §2-5 are compared to the measures published in [10] for a trombone bell.

6.1. Geometry

The bell of a trombone (Courtois 155R) has been isolated from the whole instrument. Its bore, that is its interior chamber, is described by a set of $M+1$ measured points (z_m, R_m) (see Table III). According to some instrument makers' descriptions, the discretization step used to mesh the profile is not chosen uniform but is adjusted so that its piecewise continuous affine interpolation provides an accurate description. The z-profile is displayed in Figure 10. The last segment is a piece of cone with angle $\theta_0 = 72.4°$ and the distance from its apex to its extremity is $r_0 = 0.1154\,\mathrm{m}$.

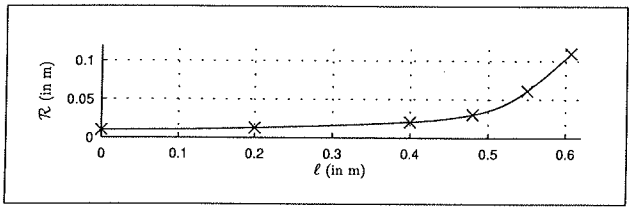

Figure 11. C^1-regular approximation with 5 Y-constant segments (-) is estimated according to [35]. *See also table IV.*

Table IV. Descriptions of the horn of a trombone Courtois 155R with C^1-regular junctions of Y-constant segments for abscissa z (top) and ℓ (bottom).

n	z_n (m)	R_n (m)	Υ_n (m^{-1})	ε_n ($m^{-\frac{1}{2}}$)	$f_c = \frac{c\sqrt{\Upsilon_n}}{2\pi}$ (Hz)
0	0	0.0104	×	×	×
1	0.2000	0.0129	11.7	0.0279	188.6
2	0.3998	0.0208	8.7	0.0194	163.0
3	0.4792	0.0298	63.8	0.0129	440.5
4	0.5404	0.0611	298.7	0.0079	953.5
5	0.5680	0.1082	758.0	0.0040	1518.9
n	ℓ_n (m)	R_n (m)	Υ_n (m^{-1})	ε_n ($m^{-\frac{1}{2}}$)	$f_c = \frac{c\sqrt{\Upsilon_n}}{2\pi}$ (Hz)
0	0	0.0104	×	×	×
1	0.2000	0.0130	11.8	0.0279	189.8
2	0.4000	0.0207	7.9	0.0194	155.2
3	0.4800	0.0302	72.3	0.0128	469.1
4	0.5500	0.0613	191.3	0.0069	763.1
5	0.6065	0.1100	45.8	0.0019	373.5

According to (6), the exact curvilinear version of this profile is given by the piecewise continuous affine interpolation of the mesh (ℓ_m, R_m) where $\ell_0 = z_0 = 0$ and

$$\ell_n = \ell_{n-1} + \sqrt{(z_n - z_{n-1})^2 + (R_m - R_{m-1})^2}, \text{ if } n \geq 1.$$

This ℓ-profile is described in Table III and displayed in Figure 10.

Using the method described in [35], accurate C^1-regular shapes are regenerated for both the z- and the ℓ- profiles, using five Y-constant segments (see Table IV and Figure 11 for ℓ).

6.2. Acoustic characteristics: measurement and models

The input impedance of the trombone bell in [10] has been measured using the experimental setup described in [55]. The measured data are displayed in Figure 12 in dashed lines, and are repeated in Figures 13–15. The calibration tests obtained in [10, § 3.1] on a reference closed straight pipe lead to the following estimates of physical constants: $\rho = 1.18\,\text{Kg/m}^3$, $c = 346.63\,\text{m/s}$. This corresponds to the "equivalent temperature" $T = 25.5°\text{C}$ (which also accounts for the effect of humidity). The coefficient of losses is computed for this temperature, from Table II $\varepsilon^\star = \sqrt{l_v} + (\gamma - 1)\sqrt{l_t} \approx 3.125 \cdot 10^{-4}\,\text{m}^{1/2}$.

For each segment n, the visco-thermal coefficients ε_n are computed as the average of ε over the segment w.r.t. the considered space variable as specifed in § 5.2. Their values are given in Table IV.

Based on these data, the normalized input impedance $Z_{in} = (1/\rho c)P_{input}/V_{input}$ and the modulus $|R_{in}^{measure} - R_{in}^{model}|$ of the deviation of the input reflection function $R_{in} = (Z_{in} - 1)/(Z_{in} + 1)$ are computed for the bore loaded by a radiation impedance. The tested configurations are summarized in Table V: model $M_\star$ is the model including all the ingredients; models Mz to $M_{\varepsilon=0}$ include all the ingredients except one; models M_{planar} and M_{CKL} correspond to "historical models"; M_{EDCG} corresponds to a model used in the recent paper [10].

6.3. Comparison

The input impedances of models of Table V are compared below. As mentioned in section 4, the contribution of the propagation models is of main importance below the cut-off frequency of the radiation impedance. For the proposed model (Z_5), based on a pulsating portion of a sphere, the dimensionless parameter ν_c corresponds to 600 Hz and the standard cutoff frequency is given by $f_c^{rad} = 848\,\text{Hz}$ (see property 5(iii)).

The critical frequency limit (9) for the validity of the propagation model which depends on the maximal radius of the bell is $f^+ = (1.84 \cdot 346.63)/(2\pi \cdot 0.11) \approx 923\,\text{Hz}$ ($> f_c^{rad}$). Moreover, the local-in-space cutoff frequency of each Y-constant segment (see remark 2) is given in Table IV.

6.3.1. Model including the four ingredients

Model $M_\star$ is based on 5 segments and gathers the 4 ingredients proposed in sections 2 to 5. The corresponding results are displayed in Figure 12.

The shapes obtained for the model and the measurement fit well, both below and above the cutoff frequency of the bell. Quantitative details are given in § 6.3.5.

6.3.2. All ingredients except one

Models Mz to $M_{\varepsilon=0}$ are based on 5 segments and gather the same 4 ingredients as in $M_\star$, except one. The corresponding results are displayed in Figure 13.

The comparison between $M_\star$ and these models shows that all of the 4 ingredients are relevant, but in different ways. The worst deviation is due to considering the z-abscissa in the Webster-Lokshin equation (Mz). Hence, it can be noticed that the inverse potential scattering methods based on the Webster equation (see e.g. [56]) could also benefit from considering the curvilinear abscissa ℓ rather than z. Using 5 cones also degrades the quality of the results, especially, beyond 1200 Hz. Significant deviations beyond $f_c^{rad} \approx 848\,\text{Hz}$ are also induced by radiation models Z_1, Z_3, Z_4. Finally, neglecting the visco-thermal losses leads to a significant deviation of the first peaks (resonance and anti-resonance).

Table V. Tested models and configurations.

Model label	Figure	abscissa	segments and junction regularity	radiation model	visco-thermal losses
$M_\star$	12 (14-15)	ℓ	5 Y-constant, C^1	Z_5	yes ($M_{\varepsilon=0}$)
Mz	13①	**z**	5 Y-constant, C^1	Z_5	yes
$M5c$	13②	$\ell(\equiv r)$	**5 cones**, C^0	Z_5	yes
MR_1	13③	ℓ	5 Y-constant, C^1	$\mathbf{Z_1}$	yes
MR_3	13③	ℓ	5 Y-constant, C^1	$\mathbf{Z_3}$	yes
MR_4	13③	ℓ	5 Y-constant, C^1	$\mathbf{Z_4}$	yes
$M_{\varepsilon=0}$	13④	ℓ	5 Y-constant, C^1	Z_5	**no**
M_{planar}	14	z	40 straight pipes, discontinuous	$\mathbf{Z_3}$	yes
M_{CKL}	14	$\ell(\equiv r)$	**40 cones**, C^0	$\mathbf{Z_4}$	yes
M_{EDCG}	15	$\ell(\equiv r)$	**40 cones**, C^0	Z_5	yes

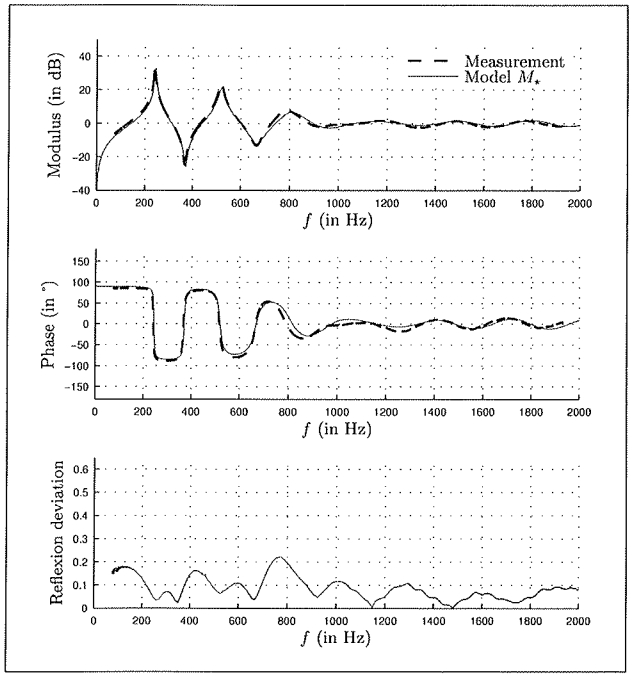

Figure 12. Normalized input impedance of the bell (modulus in dB ($20\log_{10}$) and phase in degrees) and reflection function deviation (modulus, dimensionless, linear scale): measurement (–) and model $M_\star$ (see Table V).

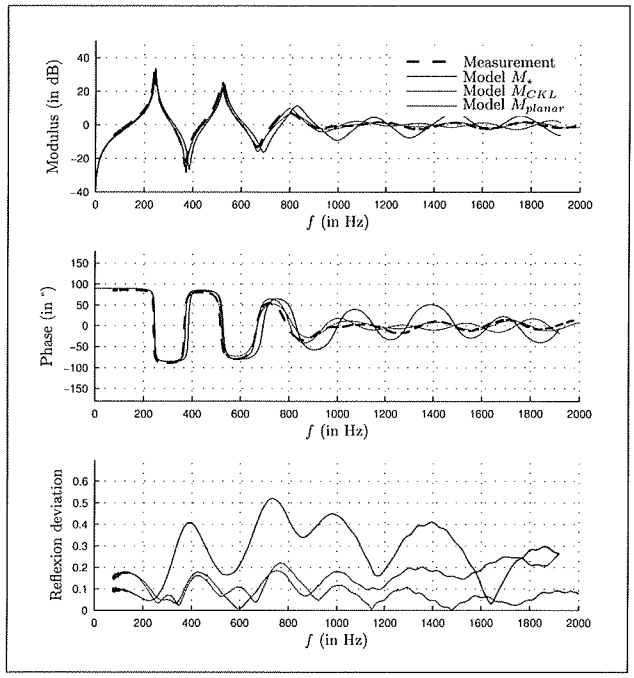

Figure 14. Comparison similar to Figure 12: measurement (–) and models $M_\star$, M_{CKL} and M_{planar}.

6.3.3. Historical models

A second list of configurations, described in table V, corresponds to "historical models", which are based on "consistent arrangements of ingredients".

Model M_{CKL} is composed of the 40 cones derived from the original profile description and the corrected version Z_4 of the Levine and Schwinger's radiation impedance, as proposed in [26]. Model M_{planar} is built with 40 lossy straight pipes and the Levine and Schwinger's radiation impedance Z_3. As displayed in Figure 14 the latter model is clearly quite poor beyond the first resonance. Model M_{CKL} is quite comparable to $M_\star$ in the low frequency range but, over $f_c^{rad} \approx 848$ Hz, it has misplaced resonances and anti-resonances.

6.3.4. Model used in the recent paper [10]

Model M_{EDCG} corresponds to a model that has been studied in [10]. It is composed of 40 cones (linking all the points measured on the trombone profile), of the radiation model Z_5 described in section 4 and includes visco-thermal losses.

As displayed in Figure 15, this model is very close to $M_\star$. In this case, the main differences are the number of segments (40 versus 5) and the associated parameters.

6.3.5. Global results and quantitative deviations

Qualitatively, the best models appear to be $M_\star$ and M_{EDCG} (as well as M_{CKL} below $f_c^{rad} \approx 848$ Hz). In these one-dimensional models, the deviations that remain visible are located in the vicinity of the cutoff frequency where both the radiation model and the 1D wave model are not accurate enough.

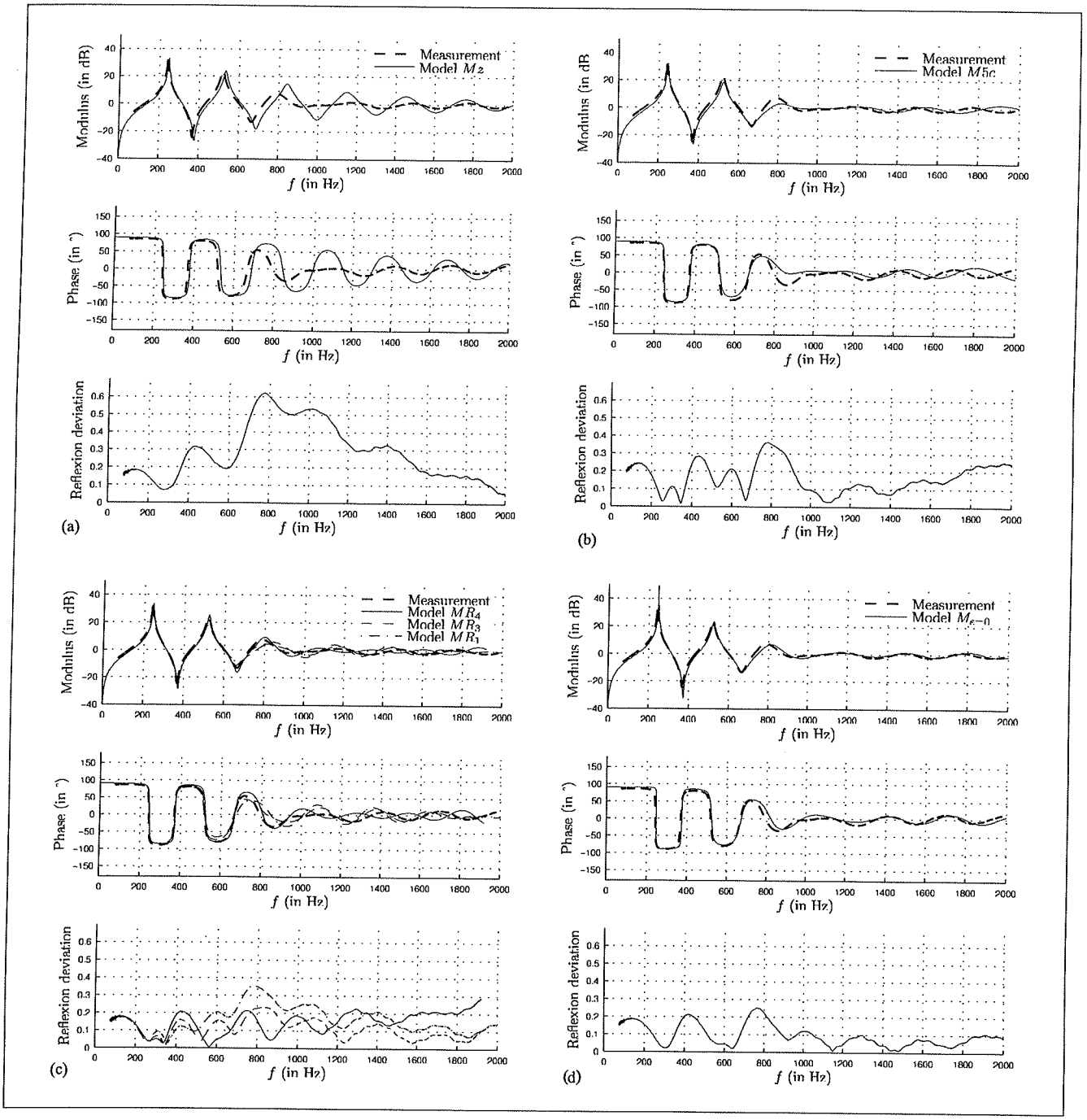

Figure 13. Comparison similar to Figure 12: measurement (–) and models including all the ingredients except one. The missing ingredient in subfigure Ⓚ is ingredient number k (models MZ to $M_{\varepsilon=0}$ are detailed in Table V). (a) Model MZ, (b) Model $M5C$, (c) Models MR_1, MR_3 and MR_4, (d) Model $M_{\varepsilon=0}$.

Out of this area, the frequencies corresponding to resonances and anti-resonances have been computed, in order to quantify the accuracy of the models. To derive accurate values, these frequencies have been chosen as the zero-crossing points of the impedance phase rather than the peaks of the impedance modulus.

The detailed values of the resonance frequencies (respectively, anti-resonance frequencies) computed for each model are given in Table VI (respectively, Table VII), as well as their deviations w.r.t. the measure.

The frequency deviations of the first resonance and anti-resonance are less than 1.2%, 1.6% and 1.8% for $M_\star$, M_{EDCG} and M_{CKL}, respectively. For the resonances and anti-resonances located over 1200Hz, deviations are less than 2.6 %, 2.6% and 7.8 %. More generally, the quantitative results on frequencies corroborate the more global and qualitative comparison made above.

It can be noticed that a frequency deviation of 1.2% is still perceptible and corresponds to about one fifth of a semi-tone (in the sense that $(2^{1/12})^{1/5} \approx 1.012$). Such a small discrepancy can be due to the model approximations

Table VI. Resonance frequencies f_k^+ of the input impedance for all the models and deviation δf_k^+ from the measure (the frequencies are computed as those for which the phase is zero and decreasing).

Model label	f_1^+ (Hz) (δf_1^+, %)	f_2^+ (Hz) (δf_2^+, %)	f_3^+ (Hz) (δf_3^+, %)	f_5^+ (Hz) (δf_5^+, %)	f_6^+ (Hz) (δf_6^+, %)
Measure	241.4	517.2	793.0	1484.2	1779.6
$M_\star$	244.3 (+1.2)	520.2 (+0.6)	818.3 (+3.2)	1487.6 (+0.2)	1800.1 (+1.2)
Mz	246.5 (+2.1)	531.6 (+2.8)	843.1 (+6.3)	1454.0 (-2.0)	1762.9 (-0.9)
$M5c$	244.1 (+1.1)	521.6 (+0.8)	860.9 (+8.6)	1551.4 (+4.5)	1922.2 (+8.0)
MR_1	243.9 (+1.0)	518.8 (+0.3)	846.3 (+6.7)	1433.0 (-3.4)	1716.5 (-3.5)
MR_3	244.3 (+1.2)	518.4 (+0.2)	827.7 (+4.4)	1450.6 (-2.3)	1748.3 (-1.8)
MR_4	244.7 (+1.4)	521.8 (+0.9)	806.7 (+1.7)	1599.8 (+7.8)	1875.4 (+5.4)
$M_{\epsilon=0}$	246.3 (+2.0)	522.6 (+1.0)	820.9 (+3.5)	1490.2 (+0.4)	1804.1 (+1.4)
M_{planar}	244.3 (+1.2)	528.0 (+2.1)	829.7 (+4.6)	1491.2 (+0.5)	1748.7 (-1.7)
M_{CKL}	245.7 (+1.8)	522.4 (+1.0)	804.1 (+1.4)	1586.6 (+6.9)	1876.0 (+5.4)
M_{EDCG}	245.3 (+1.6)	520.8 (+0.7)	814.7 (+2.7)	1477.4 (-0.5)	1794.3 (+0.8)

Table VII. Anti-resonance frequencies f_k^- of the input impedance for all the models and deviation δf_k^- from the measure (the frequencies are computed as those for which the phase is zero and increasing).

Model label	f_1^+ (Hz) (δf_1^+, %)	f_2^+ (Hz) (δf_2^+, %)	f_3^+ (Hz) (δf_3^+, %)	f_5^+ (Hz) (δf_5^+, %)	f_6^+ (Hz) (δf_6^+, %)
Measure	241.4	517.2	793.0	1484.2	1779.6
$M_\star$	371.3 (+0.8)	668.9 (+0.2)	1329.9 (-1.3)	1641.5 (+1.6)	1956.0 (+2.6)
Mz	377.6 (+2.6)	688.3 (+3.1)	1300.5 (-3.4)	1607.8 (-0.5)	1915.6 (+0.5)
$M5c$	373.5 (+1.4)	666.7 (-0.1)	1379.6 (+2.4)	1690.3 (+4.6)	1690.3 (-11.4)
MR_1	370.1 (+0.5)	674.9 (+1.1)	1292.7 (-4.0)	1573.6 (-2.6)	1843.9 (-3.3)
MR_3	371.1 (+0.8)	663.3 (-0.6)	1308.1 (-2.9)	1595.6 (-1.3)	1595.6 (-16.3)
MR_4	372.7 (+1.2)	667.5 (+0.0)	1472.4 (+9.3)	1732.1 (+7.2)	1732.1 (-9.2)
$M_{\epsilon=0}$	373.3 (+1.4)	671.9 (+0.7)	1335.5 (-0.8)	1646.7 (+1.9)	1961.2 (+2.8)
M_{planar}	384.6 (+4.5)	693.1 (+3.9)	1290.5 (-4.2)	1629.3 (+0.8)	1629.3 (-14.6)
M_{CKL}	371.7 (+0.9)	668.3 (+0.1)	1241.1 (-7.8)	1740.5 (+7.7)	1740.5 (-8.7)
M_{EDCG}	370.3 (+0.6)	669.9 (+0.4)	1362.9 (+1.2)	1658.1 (+2.6)	1951.2 (+2.3)

but also to the lack of accuracy of measurements (physical constants, geometric measurements). Additional tests on other measured bells and wind instrument resonators, as well as a sensitivity analysis could help to quantify the quality of the model.

7. Conclusions

The use of C^1-*regular junctions of* Y-*constant segments governed by the curvilinear Webster-Lokshin model* connected to the radiation impedance of a *pulsating portion of a sphere* proves to be relevant for the computation of the input impedance of brass instruments. This is the result of the 4 refinements proposed in sections 2 to 5 (in the sense that removing one of them yields worse results). More precisely, considering the curvilinear abscissa rather than the standard axial abscissa in the Webster horn equation is shown to be most important for the significantly flared parts of the bell. From the acoustical point of view, this increases the "travel length" of waves and decreases the local-in-space cutoff frequency below which travelling waves become evanescent. Moreover, combined with (C^1-regular) Y-constant piecewise approximations of the profile, this model allows preservation of the accuracy of the non approximated geometry, using only a few segments and the corresponding products of transfer matrices. The proposed radiation model improves the result in the high frequency range, corroborating the results of [10]. Finally, including visco-thermal losses in the Webster equation (Webster-Lokshin equation), which involve long-memory responses in the time-domain, improves the accuracy of the peaks of the input impedance modulus.

In summary, for flared horn, the propagation model refinements are crucial below the cutoff frequency, while the radiation model refinements are crucial beyond this cutoff frequency. However, this relevance and the validity domain have still to be characterized with measures for the case of convex pipes ($Y < 0$): the relevance of the local-in-space quasi-spherical approximation could lapse for significant bendings.

Moreover, while reducing the number of parametrized segments is not necessarily a critical point for the computation of the input impedance from profile data, it becomes one for e.g. impedance optimization tools or sound synthesis purposes. Hence, perspectives are twofolds. First, the models proposed in this paper could be used to build a toolbox dedicated to predict, estimate and optimize (w.r.t. to some computable criteria) immittances of acous-

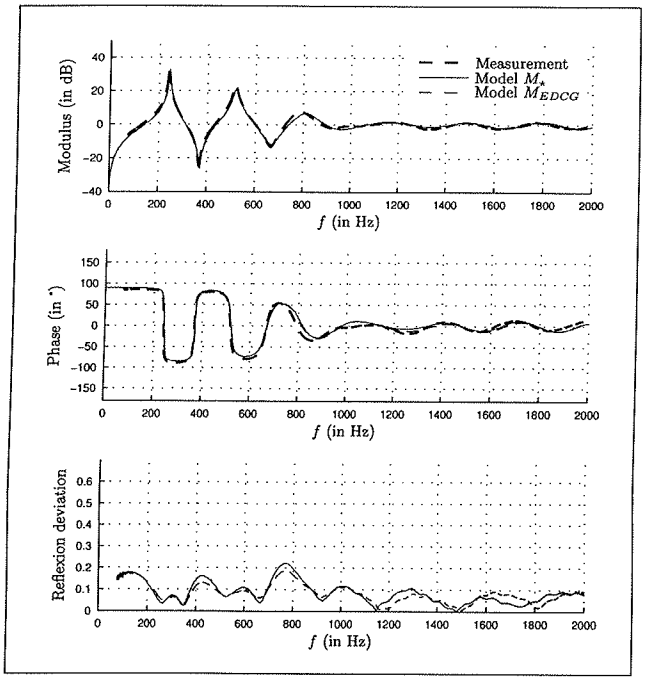

Figure 15. Comparison similar to Figure 12: measurement (–) and models $M_\star$, M_{EDCG}.

tic bores with a smooth profile and help to design horn profiles. Second, it will be used to build digital waveguides (with Kelly-Lochbaum versions) based on decompositions into decoupled waves in Y-constant segments, for realistic real-time sound synthesis purposes.

Appendix

A1. Test profile and physical constants used in this paper

The *academic* flared profile $R^\dagger$ used in sections 2-5 is chosen such that boundaries coordinates (z, R) matches with those of the trombone bell ($z_0 = 0$, $R_0 = 10.4 \cdot 10^{-3}$ m, $z^\star = 568 \cdot 10^{-3}$ m, $R^\star = 110 \cdot 10^{-3}$m), with a null slope at $z = 0$. A simple polynomial model which satisfies these properties is given by

$$R^\dagger : z \in [0, z^\star] \mapsto R_0 + \left(R^\star - R_0\right)\left(\frac{z}{z^\star}\right)^{10}. \quad \text{(A1)}$$

Moreover, physical constants are summarized in Table II. The air mass density and the sound celerity have been deduced from the calibration of the impedance sensor [55] for the measured trombone bell. They correspond to the temperature $T = 25.5$°C. Other quantities are then extracted from [24].

A2. Bell profile of a Trombone Courtois 155R

The horn profile that is measured in this paper is described in Table III. The computed corresponding parameters of the segments are given in Table IV.

Acknowledgment

The authors thank P. Eveno and R. Caussé who have furnished the measurements of the trombone, F. Silva who has furnished the Matlab code for the computation of radiation impedances Z_2 and Z_3, J. Kergomard for his helpful advice, and J.-P. Dalmont for bibliographic information.

References

[1] J. O. Smith: Physical modeling using digital waveguides. Computer Music Journal **16** (1992.) 74–91.

[2] J. L. Kelly, C. C. Lochbaum: Speech synthesis. ICA, Copenhagen, Denmark, 1962, ICA, 1–4.

[3] V. Välimäki: Discrete-time modeling of acoustic tubes using fractional delay filters. Dissertation. Helsinki University of Technology, Faculty of Electrical Engineering, 1995.

[4] G. P. Scavone: An acoustic analysis of single-reed woodwind instruments with an emphasis on design and performance issues and digital waveguide modeling techniques. Dissertation. Music Dept., Stanford University, 1997.

[5] J. O. Smith: Applications of digital signal processing to audio and acoustics. Kluwer Academic Publishers, 1998, Ch. Principles of Digital Waveguide Models of Musical Instruments, 417–466.

[6] M. V. Walstijn: Discrete-time modelling of brass and reed woodwind instruments with application to musical sound synthesis. Dissertation. University of Edinburgh, 2002.

[7] J.-D. Markel, A. H. Gray: Linear prediction of speech. Springer-Verlag, Berlin ; New York, 1976.

[8] P. R. Cook: Identification of control parameters in an articulatory vocal tract model with applications to the synthesis of singing. Dissertation. CCRMA, Stanford University, 1991.

[9] F. Silva, P. Guillemain, J. Kergomard, B. Mallaroni, A.-N. Norris: Approximation of the acoustic radiation impedance of a cylindrical pipe. Journal of Sound and Vibration **322** (2009) 255–263.

[10] P. Eveno, J.-P. Dalmont, R. Caussé, J. Gilbert: Wave propagation and radiation in a horn: Comparisons between models and measurements. Acta Acustica united with Acustica **98** (2012) 158–165.

[11] J. L. Lagrange: Nouvelles recherches sur la nature et la propagation du son. Misc. Taurinensia (Mélanges Phil. Math., Soc. Roy. Turin), 1760-1761.

[12] D. Bernoulli: Physical, mechanical and analytical researches on sound and on the tones of differently constructed organ pipes. Mém. Acad. Sci. (Paris), 1762. (in French).

[13] A. G. Webster: Acoustical impedance, and the theory of horns and of the phonograph. Proc. Nat. Acad. Sci. U.S. **5** (1919) 275–282. Errata, ibid. **6**, p.320 (1920).

[14] E. Eisner: Complete solutions of the Webster horn equation. J. Acoust. Soc. Am. **41** (1967) 1126–1146.

[15] R. F. Lambert: Acoustical studies of the tractrix horn. I. J. Acoust. Soc. Am. **26** (1954) 1024–1028.

[16] E. S. Weibel: On Webster's horn equation. J. Acoust. Soc. Am. **27** (1955) 726–727.

[17] A. H. Benade, E. V. Jansson: On plane and spherical waves in horns with nonuniform flare. I. Theory of radiation, resonance frequencies, and mode conversion. Acustica **31** (1974) 79–98.

[18] G. R. Putland: Every one-parameter acoustic field obeys Webster's horn equation. J. Audio Eng. Soc. **6** (1993) 435–451.

[19] T. Hélie: Modélisation physique d'instruments de musique en systèmes dynamiques et inversion. Dissertation. Université de Paris XI - Orsay, Paris, 2002.

[20] T. Hélie: Unidimensional models of the acoustic propagation in axisymmetric waveguides. J. Acoust. Soc. Am. **114** (2003) 2633–2647.

[21] J. Agulló, A. Barjau, D. H. Keefe: Acoustic propagation in flaring, axisymmetric horns: I. A new family of unidimensional solutions. Acustica united with Acta Acustica **85** (1999) 278–284.

[22] P. A. Martin: On Webster's horn equation and some generalizations. J. Acoust. Soc. Am. **116** (2004) 1381–1388.

[23] V. Pagneux, N. Amir, J. Kergomard: A study of wave propagation in varying cross-section waveguides by modal decomposition. part I. Theory and validation. J. Acoust. Soc. Am. **100** (1996) 2034–2048.

[24] A. Chaigne, J. Kergomard: Acoustique des instruments de musique. Belin, 2008.

[25] K. L. Kelly, C. C. Lochbaum: Speech synthesis. ICA, Copenhagen, Denmark, 1962, ICA, 1–4.

[26] R. Caussé, J. Kergomard, X. Lurton: Input impedance of brass musical instruments - comparison between experiment and numerical models. J. Acoust. Soc. Amer. **75** (1984) 241–254.

[27] L. Jordi, A. Barjau: Cas d'instruments à vent: discrétisation en tuyaux exponentiels. Journal de Physique IV **2** (1992) 79–83.

[28] L. M. B. C. Campos: Some general properties of exact acoustic fields in horns and baffles. Journal of Sound and Vibration **95** (1984) 177–201.

[29] T. Hézard: Ondes découplées et ondes progressives dans les tubes acoustiques à section variable pour la représentation en guides d'ondes. Diploma Thesis. UPMC, 2010.

[30] T. Hélie, D. Matignon: Diffusive representations for analyzing and simulating flared acoustic pipes with visco-thermal losses. Mathematical Models and Methods in Applied Sciences **16-4** (2006) 503–536.

[31] T. Hélie, R. Mignot, D. Matignon: Waveguide modeling of lossy flared acoustic pipes: Derivation of a kelly-lochbaum structure for real-time simulations. IEEE WASPAA, Mohonk, USA, 2007, 267–270.

[32] R. Mignot: Réalisation en guides d'ondes numériques stables d'un modèle acoustique réaliste pour la simulation en temps-réel d'instruments à vent. Dissertation. Edite de Paris - Telecom ParisTech, Paris, 2009.

[33] R. Mignot, T. Hélie, D. Matignon: From a model of lossy flared pipes to a general framework for simulation of waveguides. Acta Acustica united with Acustica **97** (2011) 477–491.

[34] P. M. Morse, K. U. Ingard: Theoretical acoustics. McGraw-Hill, New York, 1968.

[35] T. Hélie, T. Hézard, R. Mignot: Input impedance computation for wind instruments based upon the Webster-Lokshin model with curvilinear abscissa. ISMA, Sydney, Australia, 2010, 1–7.

[36] A. N. Norris, I. C. Sheng: Acoustic radiation from a circular pipe with an infinite flange. Journal of Sound and Vibration **135** (1989) 85–93.

[37] H. Levine, J. Schwinger: On the radiation of sound from an unflanged circular pipe. Physical Review **73** (1948) 383–406.

[38] T. Nimura, Y. Watanabé: Effect of a finite circular baffle board on acoustic radiation. J. Acoust. Soc. Amer. **25** (1953) 76–80.

[39] Y. Ando: On the sound radiation from semi-infinite circular pipe of certain wall thickness. Acustica **22** (1969-70) 219–225.

[40] W. E. Zorumski: Generalized radiation impedances and reflection coefficients of circular and annular ducts. J. Acoust. Soc. Am. **54** (1973) 1667–1673.

[41] J.-P. Dalmont, C. J. Nerderveen, N. Joly: Radiation impedance of tubes with different flanges : numerical and experimental investigation. J. Sound Vib. **244** (2001) 505–534.

[42] T. Hélie, X. Rodet: Radiation of a pulsating portion of a sphere: application to horn radiation. Acta Acustica united with Acustica **89** (2003) 565–577.

[43] G. Kirchhoff: Ueber die Einflußder Wärmeleitung in einem Gase auf die Schallbewegung. Annalen der Physik Leipzig **134** (1868) 177–193. (English version: R. B. Lindsay, ed., Physical-Acoustics, Dowden, Hutchinson and Ross, Stroudsburg, 1974).

[44] M. Bruneau, P. Herzog, J. Kergomard, J.-D. Polack: General formulation of the dispersion equation bounded visco-thermal fluid, and application to some simple geometries. Wave motion **11** (1989) 441–451.

[45] J. Kergomard: Champ interne et champ externe des instruments à vent. Dissertation. Université Pierre et Marie Curie. Thèse d'Etat, 1981.

[46] J. Kergomard: Comments on wall effects on sound propagation in tubes. J. Sound Vibr. **98** (1985) 149–153.

[47] A. A. Lokshin: Wave equation with singular retarded time. Dokl. Akad. Nauk SSSR **240** (1978) 43–46. (in Russian).

[48] A. A. Lokshin, V. E. Rok: Fundamental solutions of the wave equation with retarded time. Dokl. Akad. Nauk SSSR **239** (1978) 1305–1308. (in Russian).

[49] J.-D. Polack: Time domain solution of Kirchhoff's equation for sound propagation in viscothermal gases: a diffusion process. J. Acoustique **4** (1991) 47–67.

[50] D. Matignon: Représentations en variables d'état de modèles de guides d'ondes avec dérivation fractionnaire. Dissertation. Université de Paris XI Orsay, 1994.

[51] D. Matignon, B. d'Andréa-Novel: Spectral and time-domain consequences of an integro-differential perturbation of the wave PDE. Waves'1995, INRIA-SIAM, 1995, INRIA-SIAM, 769–771.

[52] G. Mittag-Leffler: Sur la représentation analytique d'une branche uniforme d'une fonction monogène. Acta Math. **29** (1904) 101–168.

[53] G. Dauphin, D. Heleschewitz, D. Matignon: Extended diffusive representations and application to non-standard oscillators. Proceedings of the Mathematical Theory of Networks and Systems symposium MTNS, Perpignan, France, 2000, 1–10.

[54] T. Hélie, D. Matignon: Representation with poles and cuts for the time-domain simulation of fractional systems and irrational transfer functions. Journal of Signal Processing, Special Issue on Fractional Calculus Applications in Signals and Systems **86** (2006) 2516–2528.

[55] C.-A. Macaluso, J.-P. Dalmont: Trumpet with near-perfect harmonicity: Design and acoustic results. J. Acoust. Soc. Am. **129** (2011) 404–414.

[56] B. J. Forbes, E. Pike, D. B. Sharp, T. Aktosun: Inverse potential scattering in duct acoustics. J. Acoust. Soc. Amer. **119** (2006) 65–73.